PAPER

Check for updates

Mechanistic trade-offs in dense cathode architectures for high-energy-density solid-state batteries†

Kaustubh G. Naik,[a] Carlos Juarez-Yescas, [iD] [b,c] Bairav S. Vishnugopi,[a] Saeed Moradi,[b,c] Badri Shyam,[d] Heng Yang,[d] Beniamin Zahiri,[b,c] Paul V. Braun [iD] [b,c] and Partha P. Mukherjee [iD] *[a]

As solid-state batteries (SSBs) employing Li metal anodes emerge as a promising technology for next-generation energy storage, cathodes remain a critical bottleneck, hindering further improvements in energy densities. In current state-of-the-art composite cathodes, transport constraints within the solid electrolyte (SE) network impose significant limitations on the achievable cathode active material (CAM) loading and electrode thickness. In this work, we investigate cathode design featuring densely packed, crystallographically oriented cathode crystals, free of SE and secondary phases, utilizing $LiCoO_2$ (LCO) as our model system. By examining the complex interplay between cathode microstructure, reaction-transport interactions, and chemo-mechanical phenomena underlying such dense cathodes, we evaluate their performance and identify key limiting mechanisms. We show that dense cathodes yield substantial improvements in energy density, outperforming composite cathodes by 98.7% in volumetric and 32.9% in gravimetric density at 1C. However, our findings also reveal critical interfacial, microstructural, and chemo-mechanical challenges that presently hinder the realization of their full potential. Microstructural heterogeneities in dense cathodes lead to the formation of electrochemical and mechanical hotspots during cell operation, which are identified as mechanistic pain points, impacting their rate capability, structural integrity, and cycle life. This work offers foundational insights and mechanistic guidelines for the development of high-energy-density cathodes for the next-generation SSBs.

Broader context

As the world faces a global energy crisis and intensifying climate change impacts, a swift transition to cleaner energy alternatives is the need of the hour. In response to this critical challenge, significant strides have been made in replacing gasoline-powered vehicles with electric vehicles (EVs). Lithium-ion (Li-ion) batteries, comprising a graphite anode, transition metal oxide cathode, and organic liquid electrolyte, currently lead the electric vehicle (EV) market. However, with conventional Li-ion batteries nearing their theoretical limits, meeting ever-increasing energy demands and expanding into applications like electric aviation and heavy-duty trucking requires developing new battery chemistries with higher energy densities and enhanced safety. In this regard, solid-state batteries (SSBs), employing Li metal anodes and inorganic solid electrolytes (SEs), show tremendous promise for next-generation energy storage. While significant advancements have been made in enabling stable Li metal anodes, achieving energy-dense and thick solid-state cathodes continues to remain a major challenge. This work explores a dense cathode architecture for high-energy SSBs, utilizing crystallographically oriented cathode crystals. We investigate how tailored cathode crystal orientation can facilitate rapid Li⁺ ion transport, enabling increased cathode active material (CAM) loading and enhanced energy density. However, realizing the potential of dense cathodes is predicated on addressing interfacial, chemo-mechanical, and transport challenges underlying such architectures. Through this article, we hope to provide the foundational analysis and guidelines for realizing energy-dense cathode architectures for next-generation SSBs.

[a]School of Mechanical Engineering, Purdue University, West Lafayette, IN 47907, USA. E-mail: pmukherjee@purdue.edu

[b]Department of Materials Science and Engineering, University of Illinois Urbana-Champaign, Urbana, IL 61801, USA

[c]Materials Research Laboratory, University of Illinois Urbana-Champaign, Urbana, IL 61801, USA

[d]Xerion Advanced Battery Corp, Kettering, OH 45420, USA

†Electronic supplementary information (ESI) available. See DOI: https://doi.org/10.1039/d5eb00133a

1. Introduction

The lithium (Li) metal anode offers tremendous potential to enhance the energy density of Li-ion batteries, leveraging its exceptional specific capacity (3860 mAh g⁻¹) and low electrochemical potential (−3.04 V *vs.* standard hydrogen electrode).[1–3] In pursuit of enabling Li metal anodes, solid-state batteries (SSBs) employing inorganic solid electrolytes (SEs) have emerged as a promising solution.[4–6] While significant strides have been

made in developing stable Li metal anode-based SSBs,[7–11] the solid-state cathode remains a critical bottleneck, hindering further improvements in energy density.[12–16]

In current state-of-the-art composite cathodes, which comprise intercalation-type cathode active material (CAM), a high Li^+ ion conducting SE, carbon additive, and binder, a substantial amount of SE (approximately 30 wt% or 50 vol%) is necessary to provide adequate ionic percolation pathways, thereby limiting the maximum achievable CAM loading.[17,18] While the inclusion of electrochemically inactive components, typically carbon additives and polymer binders, is necessary to facilitate electron transport and maintain mechanical integrity, respectively, their presence inevitably compromises the overall energy density of SSBs.[19,20] Beyond these limitations inherent to composite cathode architectures, additional electro-chemo-mechanical challenges arise during SSB operation.[12,21,22] The cyclic volume expansion and contraction of the CAM cause progressive contact loss at the CAM/SE interfaces, leading to the formation of solid–solid point contacts.[23–26] These point contacts act as both electrochemical hotspots, hindering cathode utilization, and stress points, causing mechanical degradation of the cathode.

Moreover, undesirable interfacial reactions such as oxidation and chemical degradation between the interacting species result in the formation of unwanted side products, leading to a loss of Li inventory and increased internal resistance, particularly under high-voltage conditions.[27–29] Such phenomena exacerbate underlying limitations, ultimately compromising the cycling performance, rate capability, Coulombic efficiency, and achievable energy density of SSBs.

To achieve high-energy-density SSBs, it is essential to maximize CAM loading in solid-state cathodes while minimizing the use of other components including SE, carbon additives, and binder, all while enhancing performance. Researchers have investigated various factors to this end, including the impact of SE ionic conductivity,[19,30,31] particle size distribution of CAM and SE,[32–35] secondary phase content,[36–38] pore fraction minimization,[39,40] and electrode heterogeneity.[41–43] Herein, we investigate a novel cathode architecture for SSBs composed of densely packed, crystallographically oriented cathode crystals, without any SE, conducting additive, or binder as shown in Fig. 1(a) (referred to as the dense cathode hereafter). With a well-defined crystal structure, layered oxide
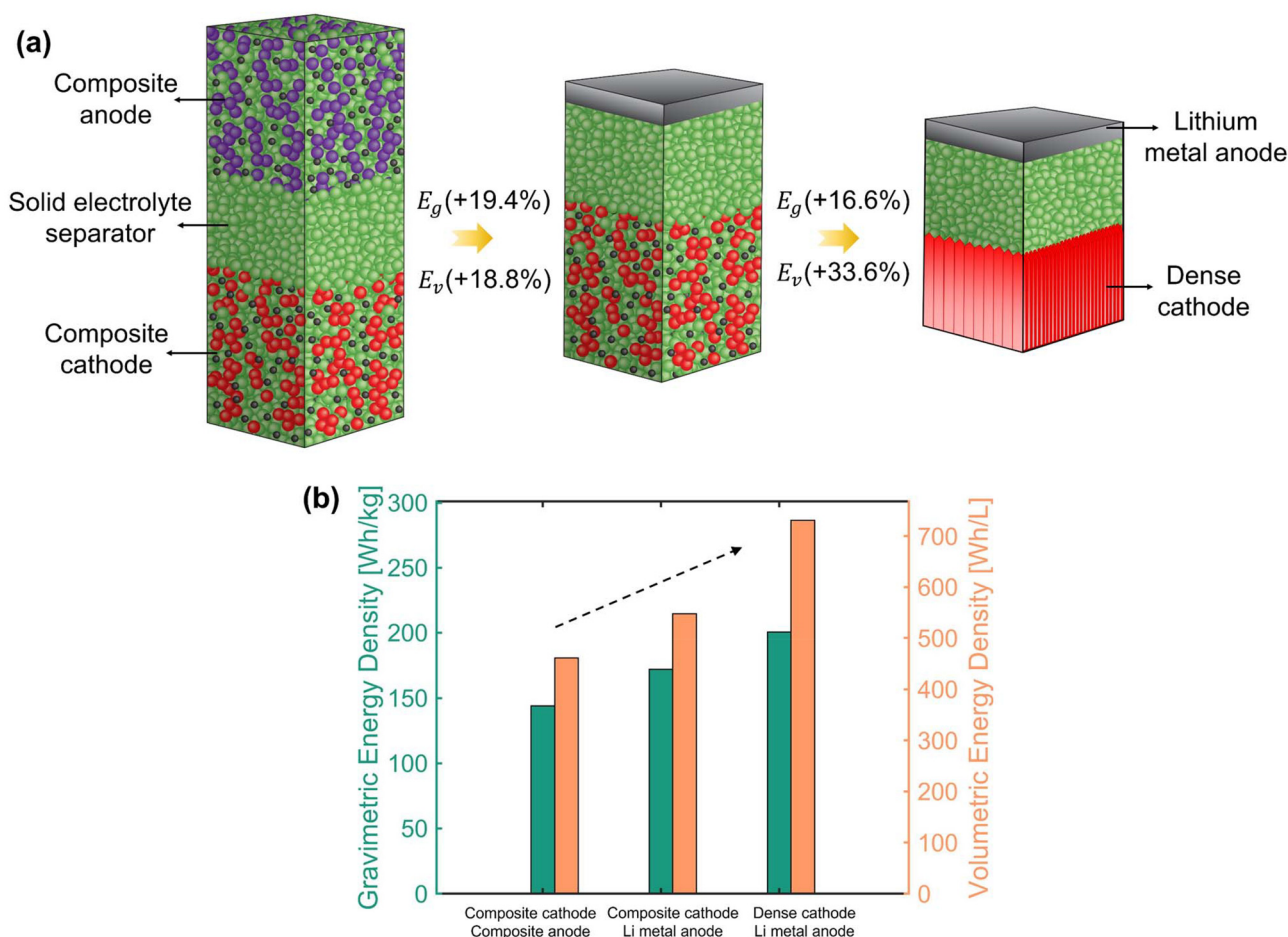

Fig. 1 (a) Schematic illustration of SSBs consisting of a composite anode and a composite cathode, a Li metal anode and a composite cathode, and a Li metal anode and a crystallographically oriented dense cathode. (b) Theoretical gravimetric and volumetric energy densities for each of these SSB designs (anode/separator/cathode basis).

cathodes such as $LiCoO_2$ (LCO) and $LiNi_xMn_yCo_zO_2$ (NMC) exhibit a preferential alignment of their Li diffusing channels, inducing anisotropy in Li transport and (de)intercalation kinetics.[44–47] In this study, we utilize LCO as our model dense cathode system, where (003) facets act as ion-blocking facets, whereas the (104) and (110) facets serve as fast-diffusing facets[48–51] for Li^+ ion transport. Therefore, by controlling crystallographic orientation such that the (003) facets are perpendicular to the current collector, LCO crystals can provide rapid transport pathways for Li^+ ions. In addition, single-crystal cathodes have been reported to exhibit sufficiently high electronic conductivity ($>10^{-4}$ S cm^{-1}).[46,47,51,52] For LCO, significantly higher electronic conductivity is achieved as soon as a small fraction of Li^+ ions is extracted from the $LiCoO_2$ structure,[53] which can be leveraged to minimize the use of conducting additives. Furthermore, restricting the CAM/SE active area to the cathode/separator interface in dense cathodes can provide greater interfacial control, minimize detrimental degradation mechanisms and interphase formation, and preserve Li inventory, thereby ensuring robust cycling performance.[48]

Despite the promise of dense cathode architectures for SSBs, a fundamental understanding of their underlying mechanisms remains largely unexplored, hindering further technological advancements. The interplay between cathode microstructure, transport phenomena, reaction kinetics, and chemo-mechanical dynamics in dense cathodes is significantly different from that in composite cathodes, necessitating an in-depth investigation. This work presents a comprehensive mechanistic landscape for crystallographically oriented, dense cathode architectures in SSBs. Employing a combined modeling and experimental approach, we thoroughly examine the performance of dense cathodes across a range of operating and design conditions, identifying key limiting regimes. By capturing the impact of inherent anisotropy resulting from crystal orientation on mesoscale interactions, this work establishes the fundamental microstructure-electrochemistry-mechanics interplay in dense cathodes. Notably, the critical role of microstructural attributes, such as interface morphology, CAM/SE contact loss, and electrode heterogeneities, in influencing cathode utilization and the spatio-temporal evolution of coupled electrochemical and mechanical signatures is analyzed, delineating key mechanistic pain points pertaining to dense cathode architectures. Finally, we present a comparative analysis of the cathode-level energy densities for composite *versus* dense cathodes, providing quantitative insights into the potential of dense cathode architectures to enhance the energy density of next-generation SSBs. Overall, this work provides fundamental insights into the mesoscale interactions underlying crystallographically-oriented dense cathode architectures, and highlights potential pathways for realizing their true potential in achieving high-energy-density SSBs.

2. Results and Discussion

Fig. 1(a) showcases schematic representations of three distinct SSB architectures, featuring: (1) a composite LCO cathode paired with a composite graphite anode, (2) a composite LCO cathode paired with a Li metal anode, and (3) a dense LCO cathode paired with a Li metal anode. Each iteration in the SSB design yields significant enhancements in the theoretical energy densities of SSBs (Fig. 1(b)). Specifically, substituting the composite anode with the Li metal anode leads to 19.4% and 18.8% increments in gravimetric (E_g) and volumetric energy (E_v) densities respectively. Replacing a composite cathode with a dense cathode can provide a further boost of 16.6% and 33.6% to E_g and E_v. The enhancements in the theoretical energy densities of the SSB can be primarily attributed to the removal of the SE and other secondary phases (conducting additives and binder), thereby maximizing the CAM loading and Li storage capacity in solid-state electrodes. It is noted that these values may vary depending on factors such as composition, thickness, and n/p ratio for electrodes. Section S1.1 of the ESI† provides all the details regarding energy density calculations.

Fig. 2 highlights the fundamental mechanisms associated with the dense cathode architecture and provides a detailed elucidation of the mechanistic differences between dense and composite cathodes. The key principle in realizing the dense cathode architecture for SSBs (Fig. 2(a)) is the potential of crystallographically oriented cathode crystals to function as mixed ion-electron conductors (MIECs), where rapid Li^+ ion transport pathways normal to fast diffusing facets ((104) and (110)) and sufficient electronic conductivity allow the elimination of the SE and conducting additives from the cathode microstructure. Here, we hypothesize that high Li diffusivity through the fast-diffusing facets not only enables long-range (electrode-scale) Li transport through the cathode microstructure, but also achieves excellent performance despite the electrochemically active area (CAM/SE contact) being constrained to the cathode/separator interface (Fig. 2(b and c)). Overall, the key mechanisms are as follows: (a) the SE separator provides transport pathways for Li^+ ions to (during discharge) or from (during charge) the cathode/separator interface, (b) reaction kinetics (Li^+ insertion/deinsertion) is confined to the cathode/separator interface, and (c) the cathode microstructure facilitates long-range solid-state diffusion of Li^+ ions as well as electron transport, enabled by crystallographically oriented LCO crystals.

These kinetic and transport interactions within dense cathode architectures are mechanistically different from those in composite cathode architectures (Fig. 2(d)). For instance, in composite cathodes, the active CAM/SE contact points are stochastically dispersed throughout the cathode bulk (Fig. 2(f)), and SE percolation within the cathode microstructure provides the necessary transport pathways for Li^+ ions to reach the CAM/SE interfaces (Fig. 2(e)). Furthermore, the lack of control over the crystallographic orientation of CAM particles limits solid-state Li^+ diffusion to a short-range phenomenon (particle-level) due to low effective Li^+ diffusivity ($\approx 10^{-11}$ cm^2 s^{-1})[54] (Fig. 2(g)). The need for SE and conducting additive phases to facilitate ion and electron transport imposes limitations on the maximum achievable CAM loading in composite cathodes. Moreover, achieving efficient ionic and electronic transport
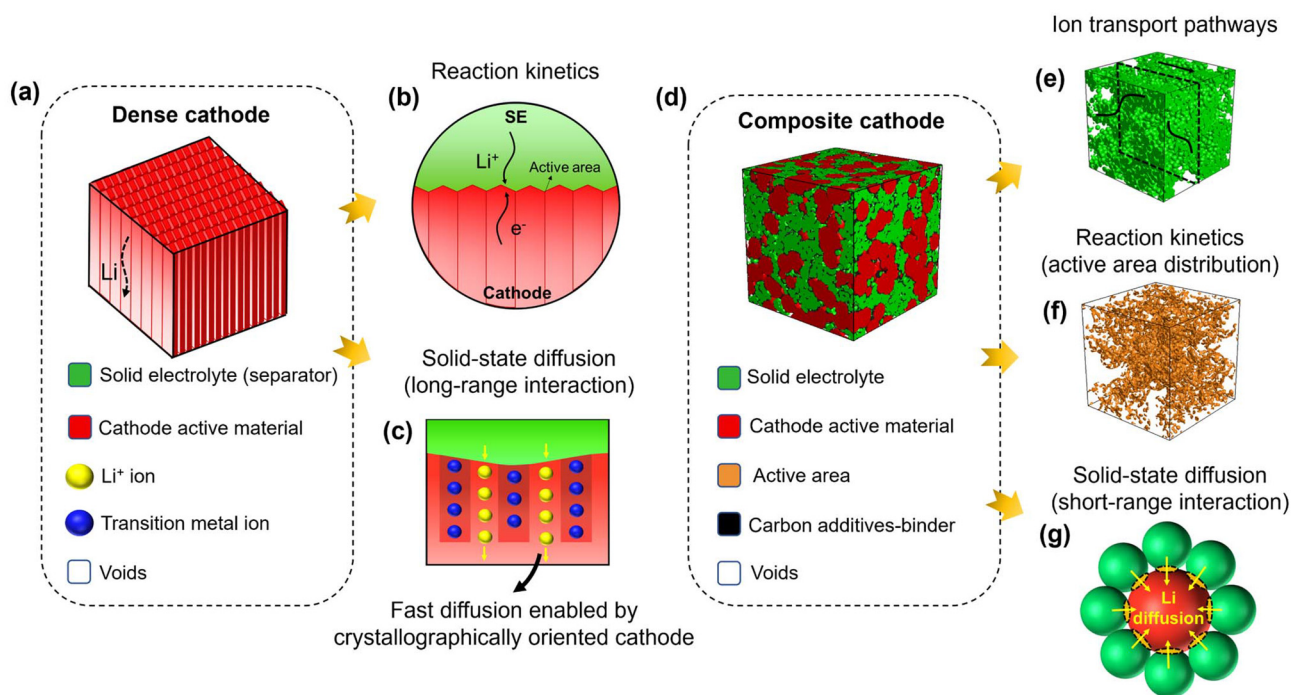
Fig. 2 Mechanistic landscape for the dense and composite cathode architectures. (a) Schematic illustration of a dense cathode architecture consisting of oriented cathode crystals along the fast-diffusing direction. (b) Reaction kinetics is restricted to the limited active area at the cathode/separator interface, followed by (c) long-range solid-state Li diffusion within the cathode microstructure which is facilitated by the crystallographic orientation of cathode crystals. (d) Schematic illustration of a composite cathode microstructure consisting of CAM, SE, CBD, and voids. Composite cathode performance is governed by coupled (e) ion transport, (f) reaction kinetics, and (g) solid-state diffusion mechanisms within the microstructure.

pathways at low stack pressures remains a significant challenge in composite cathodes. Studies[23,55] indicate that operating at low stack pressure requires either high-temperature operation, high SE content (more than 35 wt%), or sophisticated particle size configurations for CAM and SE. These complications are exclusive to composite cathodes and are not present in dense cathodes. Although dense cathode-based SSBs offer significant theoretical advantages, it is essential to examine whether this potential can be practically realized under different operating regimes, which will be expounded in the subsequent sections.

Dense cathodes in this work were fabricated by electroplating LCO crystals on an Al substrate, where the crystallographic orientation is precisely controlled by modulating the electrodeposition conditions as reported recently.[48] X-ray diffraction (XRD) patterns confirming the crystallographic orientation of the dense cathodes are shown in Fig. S1.† Fig. 3(a) and (b) display cross-sectional and top-view scanning electron microscopy (SEM) images of the dense cathode architecture, with Li-blocking (003) facets oriented largely perpendicular to the Al substrate. Cell configuration consisting of an Al current collector, a dense cathode with a 1.55 mAh cm^{-2} loading, a 250 μm thick bilayer SE separator, and Li/In as the anode (*i.e.*, counter electrode) was used (Fig. S2†). This cell design, featuring a bilayer solid electrolyte and Li/In anode, was chosen to decouple cathode behavior from anode and solid electrolyte

influences, allowing for direct investigation of cathode architecture impact on electrochemical performance. The Li/In anode was selected for its electrochemical stability and ability to suppress dendrite and void formation at the anode/solid electrolyte interface, while the bilayer solid electrolyte strategy was employed to achieve interfacial stability at both anode and cathode interfaces, thereby preventing degradation and short circuits.[48,56,57] Further details on the experimental procedure are provided in Section S2 of the ESI.† To capture the underlying mechanisms, a full-cell electrochemical performance model is developed that solves the coupled reaction kinetics, ion/electron transport, and solid-state Li$^+$ diffusion within the system (Fig. S3†). Section S3 of the ESI† provides the mathematical framework and associated details. Fig. 3(c) presents the discharge profiles obtained for different C-rates from both experiments and the model, demonstrating excellent agreement between the two. While the model is validated for experimental cell design, its applicability extends to ideal solid-state cell configurations, comprising dense cathodes, thin SE separators, and Li metal anodes, the analysis for which is presented in Fig. S4.†

The validated model is employed to investigate the performance of dense cathodes under various operational and design scenarios. Fig. 3(d) illustrates the impact of C-rate and cathode thickness on the attainable cathode-specific capacities. As both C-rate and cathode thickness increase, the discharge
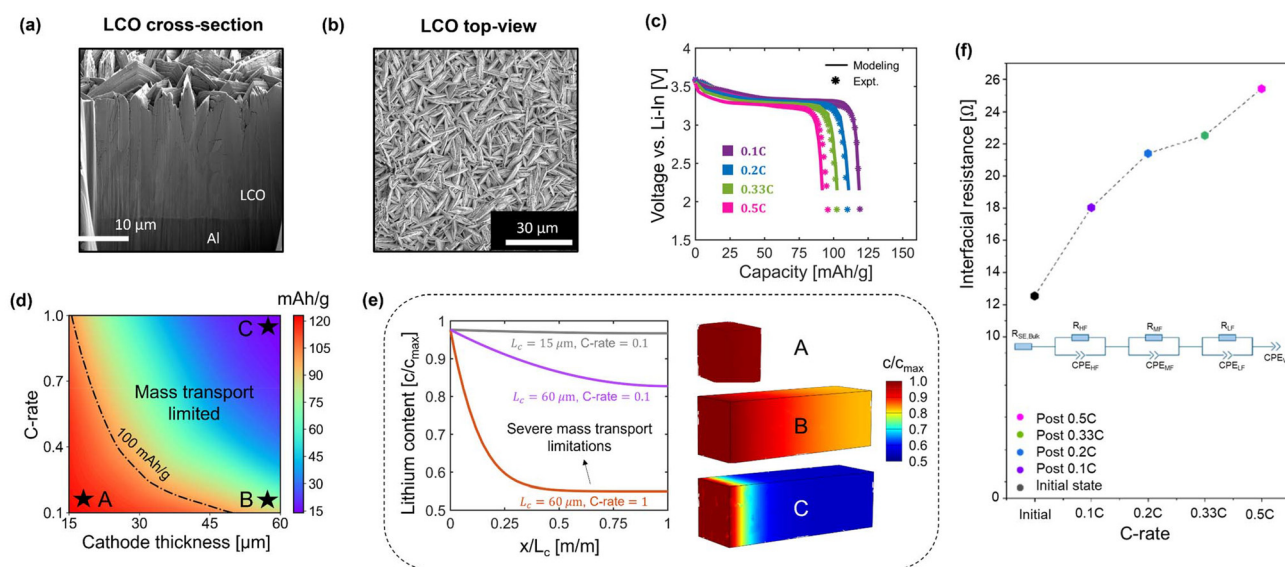
Fig. 3 SEM images of the dense cathode microstructure with Li-blocking (003) facets aligned perpendicular to the substrate: (a) cross-section and (b) top view. (c) Discharge profiles obtained from modeling and experiments for different C-rates showing an excellent match. (d) Discharge capacity as a function of C-rate and cathode thickness. (e) Li concentration across the cathode depth for the three different cases marked as A, B, and C in (d). (f) Interfacial resistance obtained using electrochemical impedance spectroscopy (EIS) after different C-rates during rate capability tests. The LCO/SE interfacial resistance is characterized by the mid-frequency features in the EIS Nyquist plot.

capacity decreases due to mass transport limitations within the dense cathode. Unlike composite cathodes, where performance at high rates and thicknesses is primarily limited by ion transport limitations in the SE phase,[17,58] the performance of dense cathode architectures is constrained by solid-state Li^+ diffusion. A contour line indicating 100 mAh g^{-1} in Fig. 3(d) demarcates the transition from a non-limiting to a mass transport limited regime as C-rate and thickness increase. Fig. 3(e) shows the Li concentration profiles across the cathode depth at the end of discharge for three distinct cases (A, B, and C), as marked in Fig. 3(e). Here, the Li concentration and cathode depth are represented as nondimensional numbers, where c_{max} and L_c are the maximum Li concentration and cathode thickness, respectively. The mass transport limitations for case B (high thickness) and case C (high thickness and C-rate) lead to localized concentration buildup near the cathode/SE interface, causing elevated kinetic overpotential and a rapid voltage drop, thereby restricting rate capability and achievable cathode thickness. Notably, the validated model suggests that the effective Li diffusivity in the dense cathode ($D_{eff} = 1.5 \times 10^{-9}$ cm^2 s^{-1}) is much lower than the intrinsic diffusivity of the fast-diffusing facets (with values reported as high as 10^{-7} cm^2 s^{-1} in the literature[44,59,60]). This discrepancy can be attributed to the deleterious impact cathode microstructure and associated heterogeneities have on Li transport and underlying limitations, emphasizing the need for a thorough investigation into these factors, which will be conducted in the subsequent sections.

The rate capability tests were complemented with electrochemical impedance spectroscopy (EIS) to probe interfacial

impedance characteristics of dense cathodes at different C-rates (Fig. 3(f) and Fig. S5†). The LCO/SE interfacial resistance, characterized by mid-frequency features, is used to monitor the interface impedance. The interfacial resistance exhibits a consistent and notable increase as the cell is cycled at higher current density. This result suggests that the cathode/SE interfacial delamination is exacerbated at higher rates. In dense cathode architectures, where the electrochemically active area is already limited and exclusively localized at the cathode/separator interface, and not distributed throughout the cathode bulk, the loss of interfacial contact can have far-reaching consequences for the reaction-transport dynamics, impacting the cathode performance. To investigate this aspect further, non-contact zones at the cathode/SE interface are incorporated in the developed model, as schematically illustrated in Fig. 4(a). Fig. 4(b) shows the Li concentration distribution within the cathode at the end of 0.25C discharge for contact fractions (A/A_t) of 1, 0.8, and 0.6, where A represents the actual active area and A_t denotes the maximum theoretical contact area. With the decrease in the contact fraction, the overall utilization of the cathode is significantly compromised. Current focusing at contact points not only increases the kinetic overpotential but also causes severe underutilization of the cathode regions directly in front of the non-contact zones, leading to pronounced heterogeneity in lithiation behavior and reduced overall performance. Such a phenomenon is attributed to the inherent anisotropy in the Li^+ transport properties of LCO crystals[61] (Fig. 4(a)). To elaborate, the lithiation of LCO crystals directly in front of the non-contact zones requires bulk Li diffusion parallel to the interface (i.e., in
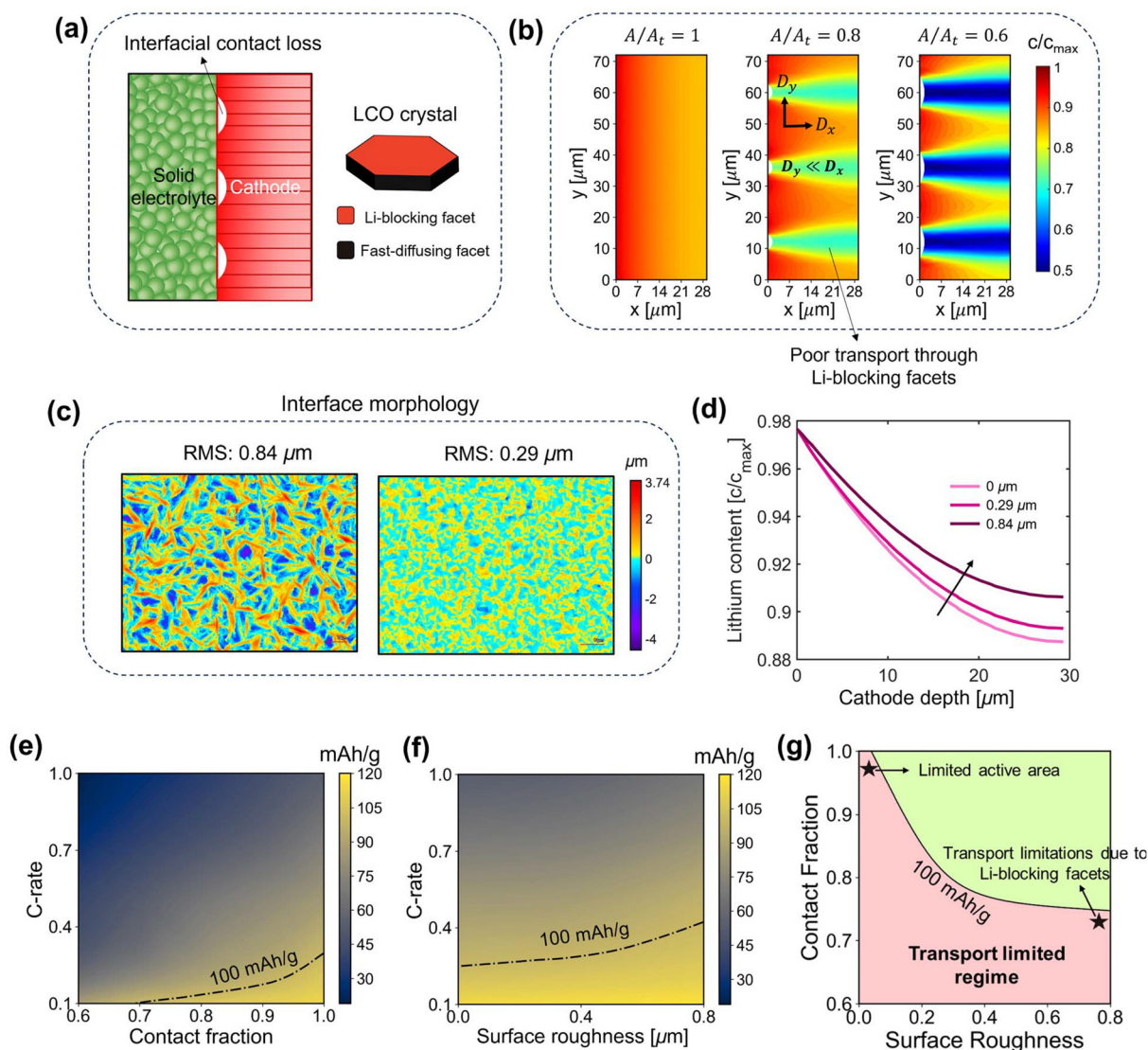
© 2025 The Author(s). Published by the Royal Society of Chemistry

Fig. 4 (a) Schematic depicting the interfacial contact loss at the cathode/SE interface. Contact loss coupled with the inherent anisotropy stemming from the crystallographic orientation can profoundly impact the cathode performance. (b) Effect of interfacial contact loss on the lithiation behavior. (c) Interface morphologies of the rough and smooth cathode/SE interfaces. (d) Effect of interfacial surface roughness (represented as the root mean square (RMS) value) on the electrochemical utilization across the cathode depth at the end of discharge at 0.25C. (e) Discharge capacities as a function of C-rate and contact fraction. (f) Discharge capacities as a function of C-rate and surface roughness. (g) Limitation regime map as a function of contact fraction and surface roughness for 0.25C discharge.

y-direction from high to low concentration *via* Li-blocking facets). However, the extremely low Li$^+$ diffusivity (D_y) through the Li-blocking facets impedes this Li$^+$ transport, leading to severe underutilization in these regions (Fig. 4(b)).

To experimentally verify the impact of Li-blocking facets on transport limitations, dense cathodes were fabricated with Li-blocking (003) facets oriented parallel to the Al current collector. Fig. S1 of the ESI† presents the corresponding XRD profiles. Fig. S6† shows the top-view SEM images and compares the electrochemical performance of such a cathode with the cathode discussed in Fig. 3 for SSBs. Consistent with our hypothesis, significantly inferior performance is achieved, primarily due to severe transport limitations imposed by the Li-

blocking facets of the LCO crystals. Previous study has reported similar findings, with vertically aligned diffusion planes showing full utilization, while parallel configurations limited electrochemical activity to the LCO surface.[44] Further analysis of the impact of orientation on dense cathode performance is presented in Section S5 of the ESI.†

The electrochemically active area in dense cathode architectures is also strongly influenced by the morphology of the cathode/SE interface. To examine the impact of interface morphology, the dense cathodes were fabricated with tailored interface morphologies (rough and smooth), and laser profilometry was utilized to characterize the interface as shown in Fig. 4(c). The surface roughness, expressed as the root mean

square (RMS) value, was found to be 0.84 μm for the rougher interface and 0.29 μm for the smoother one. The cathode with a rough interface exhibited a remarkably higher active area, almost four times that of the ideal flat interface. The relationship between surface roughness and the active area is summarized in Table S3 of the ESI.† Experimental charge/discharge profiles for both cases (Fig. S8†) reveal enhanced performance for the dense cathode with the rough interface. To shed light on the underlying mechanisms, a rough interface was incorporated into the model, and Fig. 4(d) displays Li concentration profiles across the cathode depth at the end of 0.25C discharge for interface roughness values of 0, 0.29, and 0.84 μm. An increase in surface roughness results in improved cathode utilization. Mechanistically, the increased active area at higher surface roughness reduces local reaction current densities at the interface. Consequently, the reduced overpotential for the redox reaction at the cathode/SE interface enhances overall cathode utilization.

To investigate the impact of interfacial attributes on rate capability, Fig. 4(e) and (f) show the discharge capacities as the function of C-rate and contact fraction, and C-rate and surface roughness, respectively. The transport and reaction limitations triggered by the contact loss are observed to exacerbate with increasing C-rate. For example, at 1C, capacity drops from 60 mAh g^{-1} to 19 mAh g^{-1} (a 68% reduction) as the contact fraction decreases from 1 to 0.6, whereas at 0.1C, capacity decreases from 115 mAh g^{-1} to 87 mAh g^{-1} (24% reduction). This underscores the critical role of the in-plane Li$^+$ transport (parallel to the interface) in the rate capability of the dense cathode, especially in scenarios where interfacial delamination occurs. In this regard, fine-tuning the applied stack pressure could play a crucial in mitigating these limitations for the dense cathodes. Increasing the surface roughness of the interface can partially alleviate these challenges as seen in Fig. 4(f). Unlike Li metal anodes, where the rough interface morphology triggers electrodeposition heterogeneity, leading to instabilities such as dendrite growth,[62,63] the rough interface has a positive influence on the dense cathode performance.

To sum up, the limitation regime map as a function of contact fraction and surface roughness is presented in Fig. 4(g) for 0.25C discharge. For a smoother interface (*e.g.*, surface roughness < 0.1 μm), even if intimate contact is achieved (*e.g.*, contact fraction ~1), the performance is compromised due to limited CAM/SE active area, which causes increased local reaction current density and elevated kinetic overpotential. Such a scenario is highlighted in Fig. 4(g) by a black marker. Enhancing interfacial roughness increases the active area, leading to improved cathode performance. Nevertheless, maintaining CAM/SE contact remains vital, as loss of contact can induce transport limitations within the cathode bulk due to hindered diffusion through Li-blocking facets (as denoted by the black marker in Fig. 4(g)). Overall, the analysis in Fig. 4 highlights the critical importance of co-optimizing the microstructural (*i.e.*, interface morphology) and operating conditions (*e.g.*, stack pressure for mitigating the

interfacial contact loss) for realizing dense cathode-based SSBs.

The high energy density potential of dense cathode architectures is predominantly contingent upon optimal crystallographic orientation, making it crucial to maintain the cathode's mechanical and structural integrity throughout prolonged cycling. Fig. 5(a) shows the cycling performance of an SSB with a dense LCO cathode cycled at 1C and room temperature, while Fig. 5(b) presents the post-cycling focused ion beam (FIB)-SEM cross-section of the dense cathode. Unlike the pristine dense cathode (Fig. 3(a)), which exhibits no significant cracks, the cycled dense cathode displays extensive cracking throughout its cross-section, with cracks extending to the Al substrate. It is hypothesized that factors including volume changes of the LCO and the presence of microstructural defects can lead to the formation of stress hotspots, thereby impacting the mechanical stability of the cathode.

To evaluate this complex microstructure–electrochemistry–mechanics interplay, a microstructure-aware chemo-mechanical modeling study is conducted to examine the spatiotemporal evolution of electrochemically-induced stresses within the cathode. All modeling details and the mathematical framework are provided in Section S3 of the ESI.† The model domain considered is schematically illustrated in Fig. 5(c), which incorporates all relevant microstructural features, including oriented and disoriented LCO crystals, pores/microcracks, and interfacial heterogeneities (contact/noncontact zones). Fig. 5(d) depicts the spatiotemporal evolution of Li concentration within the cathode during the 1C discharge operation. The intrinsic anisotropy stemming from crystal orientation, coupled with microstructural irregularities, induces localized transport limitations within the cathode microstructure, resulting in pronounced heterogeneity in lithiation behavior. Such a phenomenon not only limits the achievable utilization and energy density, but also leads to the generation of nonuniform stresses within the system, as shown in Fig. 5(e) and (f). These highly nonuniform stresses intensify with progressive lithiation, and the sites with microstructural defects including pore/microcrack tips and interfacial void edges serve as tensile stress hotspots, potentially imperiling the structural integrity of the dense cathode. Subsequently, the mechanical failure within the cathode and at the cathode/SE interface can critically impact Li$^+$ diffusion and reaction kinetics, thereby exacerbating the rate and cycling performance of SSBs.

The chemo-mechanical degradation mechanisms established *via* modeling can be directly linked to the experimental findings reported in Fig. 5(a) and (b). In particular, the experiments suggest that the mechanical fracture within the cathode bulk and contact loss at the LCO/SE interface compound and accelerate the capacity fade with cycling. For instance, the accessible capacity drops from 86 mAh g^{-1} to 81 mAh g^{-1} after 25 cycles (5.8% decrease), whereas it drops to 62 mAh g^{-1} (27.9% decrease) and 34 mAh g^{-1} (60.5% decrease) after 50 and 75 cycles respectively. As fracture occurs with cycling and Li$^+$ transport is hindered through cracks as well as Li blocking facets of the LCO crystals, it nonlinearly impacts the cycling
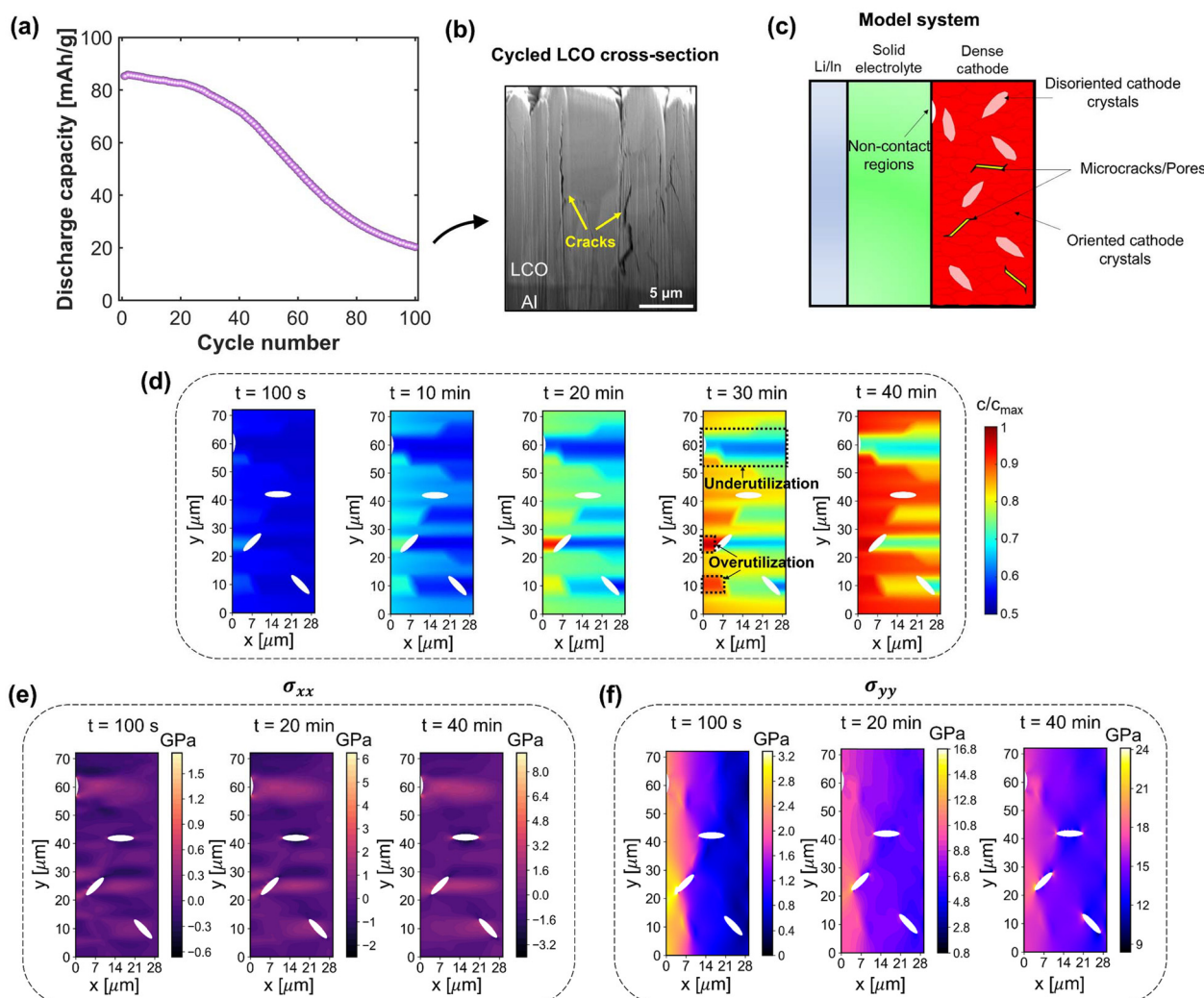
Fig. 5   (a) Cycling performance of SSB with dense LCO cathode obtained for 1C, room temperature operation. (b) FIB-SEM cross-section of cycled LCO indicating significant cracking. (c) The model system with microstructural heterogeneities considered to study the chemo-mechanical phenomena in dense cathode architectures. Spatiotemporal evolution of (d) the Li concentration, normal stresses in (e) x and (f) y directions within the dense cathode during 1C discharge operation.

performance, exhibiting an initial gradual decline followed by a steep drop in capacities. The schematic illustration depicting the impact of microstructural heterogeneities on chemo-mechanical degradation and cycling performance is presented in Fig. 6(a). In composite cathodes, the presence of more compliant phases such as solid electrolyte, binder, and carbon additives can potentially help in accommodating the volume changes in the cathode material, enabling better cycling performance.[64] On the other hand, the dense cathode architecture consists of 100% cathode loading, with no other phases. Such architectural characteristics of the dense cathode result in much higher stresses, potentially leading to higher degrees of mechanical degradation.

The model was further employed to investigate the impact of C-rate on lithiation and stress evolution (Fig. 5(d–f) and Fig. S9, S10†). Results show that electrochemical and mechanical hotspots intensify with increasing C-rate. Notably, this finding is consistent with the experimentally observed rise in interfacial resistance at higher C-rates (Fig. 3(f)). The chemo-mechanical response of the dense cathode, characterized by uneven volume changes and tensile stress hotspots at the cathode/SE interface, likely exacerbates delamination at higher C-rates.

It is worth noting that the orientation of defects plays a crucial role – those perpendicular to the current collector have negligible effects on Li$^+$ transport and degradation, whereas parallel microcracks exhibit maximum impact. A previous study has shown that cracks in single-crystal LCO predominantly propagate along the Li-blocking (003) plane.[65] This implies that achieving precise control over LCO crystal orientation in dense cathodes would not only enhance Li transport via fast-diffusion facets but also favor crack propagation perpendicular to the current collector, minimizing performance degradation.

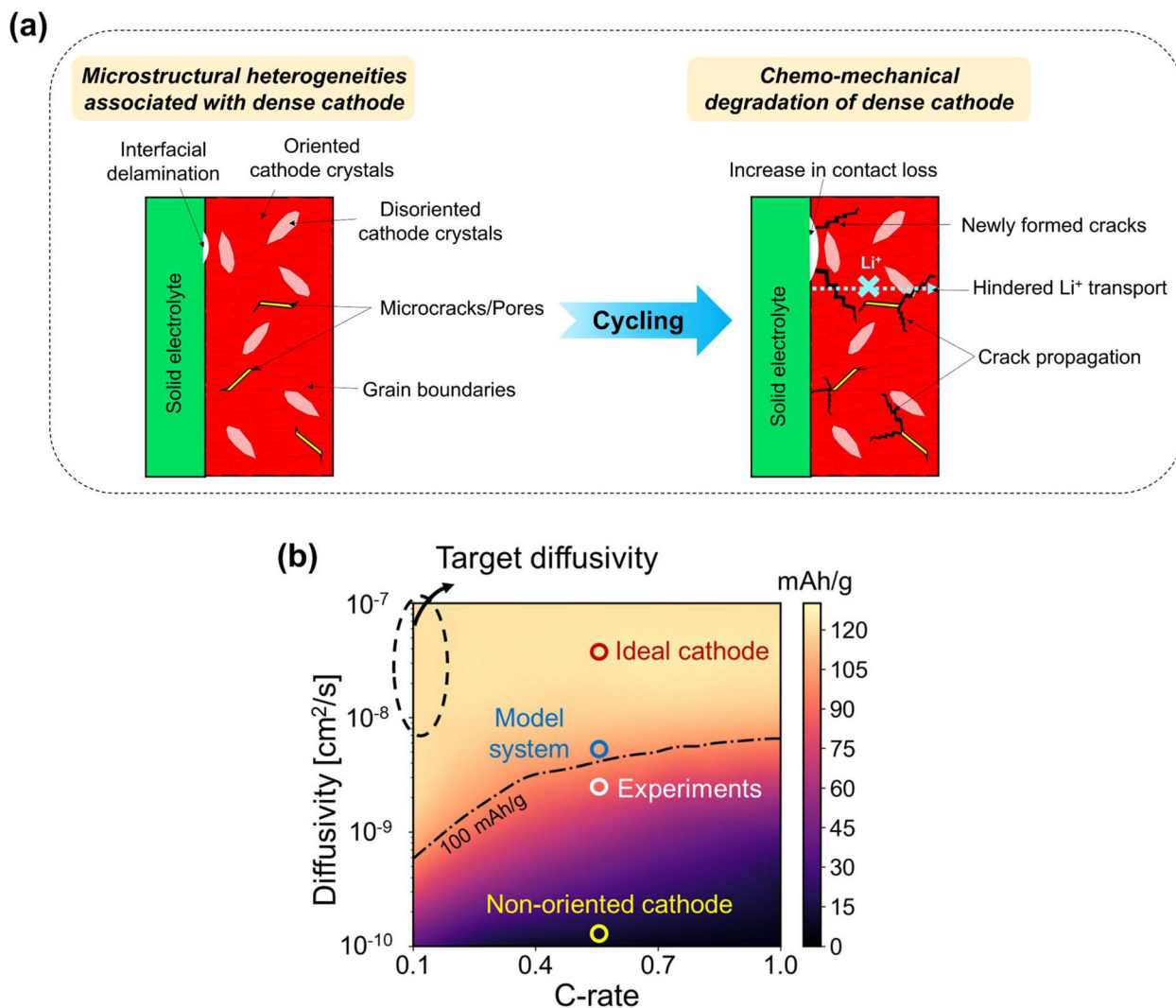**Fig. 6** (a) Schematic illustration of the microstructural heterogeneities associated with the dense cathode architectures in SSBs, followed by their impact on the chemo-mechanical degradation of dense cathode with cycling and its implication on Li transport. (b) Discharge capacity map as a function of effective diffusivity and C-rate, with markers indicating the position of various dense cathode architectures considered.

The transport limitations arising from interfacial (contact loss, low surface roughness) and bulk (crystal orientation, pore formation, and microcracking) phenomena, as discussed in Fig. 4 and 5, can be theoretically interpreted in terms of the effective Li diffusivity (D_{eff}) of the dense cathode. The collective influence of various microstructural attributes and chemo-mechanical degradation on the electrochemical performance can be quantitatively encapsulated by D_{eff}. This provides a unified metric to analyze the underlying limitations in dense cathode architectures, as presented in Fig. 6(b). Here, we examine four distinct dense cathode architectures: an idealized cathode, a model cathode system (considered in Fig. 5), a dense cathode synthesized in this work (presented in Fig. 3), and a non-oriented dense cathode (*i.e.*, a dense cathode with randomly oriented cathode crystals). An idealized cathode is defined as a cathode with a flawless microstructure and properties the same as those of the single crystal LCO. Notably, a

high D_{eff} enables maximum capacity achievement even at elevated C-rates (*e.g.*, 1C), indicating that the idealized dense cathode can achieve near-full utilization with negligible transport limitations. Such an ideal cathode can be regarded as the benchmark for assessing the dense cathode's performance, providing a reference point to quantify the deviations in D_{eff} and achievable capacities from an optimal scenario. In contrast, a non-oriented dense cathode, characterized by randomly oriented LCO crystals without preferential crystallographic alignment, establishes a lower baseline for evaluating dense cathode performance. Here, a low D_{eff} ($\sim 10^{-10}$ cm^2 s^{-1}) significantly limits capacity achievement, even at low C-rates (*e.g.*, 0.1C) due to the severe transport limitations within the cathode. The dense cathode synthesized in this work and the model cathode system presented in Fig. 5 exhibit intermediate performance signatures, falling between the idealized and non-oriented cathodes with D_{eff} of 1.5×10^{-9} cm^2 s^{-1} and $4 \times$

10^{-9} cm^2 s^{-1}, respectively. In this regime of Li diffusivity, cathode performance exhibits a pronounced C-rate dependence, where enhanced performance is attained at lower C-rates, while transport limitations at elevated rates substantially compromise achievable capacities. The reduced D_{eff} of the experimental cathode, relative to the ideal case, can be attributed to microstructural defects, heterogeneities, and chemo-mechanical degradation. Notably, the model cathode system (Fig. 5) exhibits a higher D_{eff} than the experimental cathode, indicating that the severity of imperfections manifested in experiments exceeds those accounted for in the model system in Fig. 5. Overall, the analysis presented here highlights the critical role of cathode design optimization to unlock the full cathode capacity and to mitigate the impact of chemo-mechanical degradation inherent to dense cathode architectures, thereby enhancing their performance and cycle life.

While this is the case for SSBs, it is important to highlight the disparity with liquid electrolyte-based systems. Fig. S11† shows the comparison of dense cathode performance in SSB *versus* liquid electrolyte-based system where enhanced rate capability is observed in liquid electrolyte cell. Additionally, the dense cathode shows excellent cycling performance in liquid electrolyte system (Fig. S12†). The disparity primarily lies in the nature of the electrode/electrolyte interfaces. In liquid electrolyte systems, conformal contact is established at the cathode/electrolyte interface, and the liquid electrolyte infiltrates the cathode bulk, providing an additional ion transport network and electrochemically active sites. This also reduces the required Li diffusion lengths within the cathode, thereby mitigating the diffusion limitations observed in solid-state systems and leading to enhanced battery performance. In contrast, limited solid–solid contact, contact loss during battery operation and inability of solid electrolyte to seep into the cathode bulk collectively hinders the rate performance of solid-state battery when compared with liquid counterparts.

Fig. 7 provides a comparative analysis of the electrochemical performance of composite and dense cathodes. To evaluate the performance of the composite cathode, an electrochemical performance model is employed that solves coupled reaction kinetics, ion/electron transport, and solid-state Li diffusion within the cathode microstructure, as reported previously.[23,41] Fig. 7(a) and (b) compare the CAM-specific capacities (mAh g^{-1}) of composite cathodes exhibiting various CAM wt% to that of a dense cathode for 0.1C and 0.5C, respectively. In this analysis, the total CAM amount is held constant across all cathode compositions, matching the amount used in the dense cathode (fabricated in Fig. 3). The composite cathode thickness is then evaluated according to the CAM wt% (Table S4†).

At a low C-rate of 0.1C (Fig. 7(a)), composite cathodes exhibit high capacities (~120 mAh g^{-1}) even at CAM loadings as high as 90 wt%, indicating minimal electrochemical limitations. However, further increasing the CAM content above 90 wt% results in a sharp decline in accessible capacity. This can be attributed to severe ion transport limitations due to

increased tortuosity in the SE percolation network, as well as reduced CAM/SE active sites due to insufficient SE phase. On the other hand, as the C-rate is increased to 0.5C, high capacities are achieved only up to 70 wt% CAM, beyond which further increase in CAM content results in a steep drop in the capacities, plummeting to near zero for 90 wt% CAM and above (Fig. 7(b)). At higher C-rates, ion transport limitations are triggered at much lower CAM content, imposing stricter limits on the maximum achievable CAM loading for high-rate applications in SSBs. In contrast, the dense cathode architecture (100 wt% CAM) achieves 119 mAh g^{-1} and 97 mAh g^{-1} capacity under the same conditions of 0.1C and 0.5C respectively. This enhanced performance is attributed to the improved Li$^+$ diffusion facilitated by the crystallographically oriented LCO crystals. Unlike composite cathodes, where high-rate performance is predominantly limited by ion transport, the reduced accessible capacity in dense cathodes at higher C-rates stems from inherent diffusion limitations. The corresponding Li concentration profiles at the end of 0.5C discharge for the composite cathodes with 60 wt% and 80 wt% CAM and dense cathode are shown in Fig. 7(e). Comparisons between dense and composite cathodes at additional C-rates (0.2C, 0.33C, and 1C) are provided in Fig. S13(a–c) of the ESI.†

Fig. 7(c, d) and Fig. S13(d–f)† illustrate how the CAM-specific capacities of the composite and dense cathode architectures translate to electrode-level volumetric and gravimetric energy densities across various C-rates. Although composite cathodes deliver high CAM-specific capacities up to a certain CAM content for each C-rate, the presence of a high amount of SE and other secondary phases (*e.g.*, conducting additives and binder) reduces the electrode-level energy densities compared to dense cathodes.

A notable trend is observed in composite cathodes as a function of C-rate. At a low C-rate of 0.1 (Fig. 7(c)), the delivered energy densities increase monotonically up to 90 wt% CAM content, where the maximum gravimetric and volumetric energy densities reach 408.5 Wh kg^{-1} and 1678 Wh L^{-1}, respectively. At higher C-rates, however, energy densities exhibit a non-monotonic trend with increasing CAM content. For example, at 0.2C and 0.33C, energy densities peak at 80 wt% CAM content, followed by a decline at 90 wt% CAM (Fig. S13(d and e)†). Furthermore, this trend becomes more pronounced at even higher C-rates, with energy densities peaking at 70 wt% CAM for 0.5C (Fig. 7(d)) and 1C (Fig. S13(f)†), followed by a dramatic drop at 80 and 90 wt% CAM content due to severe ion transport limitations. The maximum energy densities delivered by the composite cathode at 0.5C and 1C are 309 Wh kg^{-1} and 992 Wh L^{-1}, and 237 Wh kg^{-1} and 760 Wh L^{-1}, respectively.

Most importantly, the dense cathode architecture showcased in this work surpasses the maximum energy densities delivered by the composite cathode across all considered C-rates (0.1C to 1C). In particular, dense cathode exhibits gravimetric and volumetric energy density of 447 Wh kg^{-1} and 2143 Wh L^{-1} at 0.1C (Fig. 7(c)), representing increases of 9.42% and 27.7%, respectively. At higher C-rates, the dense cathode deli-
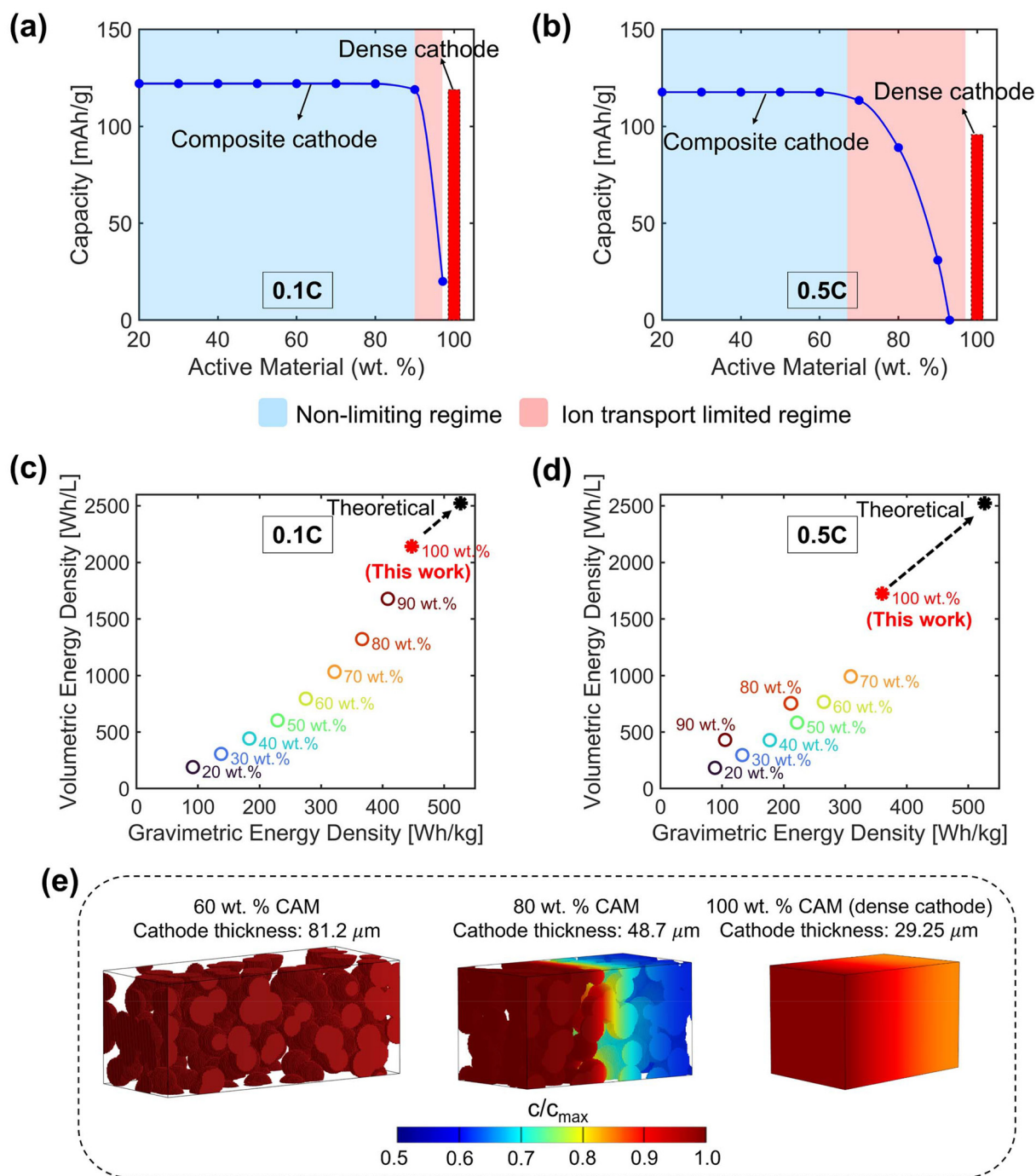
Fig. 7 Comparison of CAM-specific capacity for dense cathode and composite cathodes with varying CAM content at (a) 0.1C, and (b) 0.5C. Electrode-level volumetric and gravimetric energy densities delivered by dense cathode and composite cathodes with varying CAM content at (c) 0.1C, (d) and 0.5C. The theoretical (or target) value denotes the maximum energy density possible for a dense cathode (obtained by considering 140 mAh g^{-1} as the theoretical CAM-specific capacity for LCO). (e) Li concentration profile within the composite cathodes with 60 wt% and 80 wt% CAM contents and dense cathode at the end of discharge for 0.5C.

vers energy densities of 360 Wh kg^{-1} (16.5% increase) and 1724 Wh L^{-1} (73.7% increase) at 0.5C (Fig. 7(d)), and 315 Wh kg^{-1} (32.9% increase) and 1510 Wh L^{-1} (98.7% increase) at 1C (Fig. S13(f)†), demonstrating substantial improvements over composite cathodes. The idealized dense cathode's energy

densities (2521 Wh L^{-1} and 526 Wh kg^{-1}), denoted by a black marker in Fig. 7(c) and (d), set the theoretical benchmark for dense cathode architectures, offering opportunities for further enhancement in both volumetric and gravimetric energy densities.

In summary, dense cathode architectures present tremendous potential for achieving high energy density SSBs. This work is also expected to guide future research efforts in optimizing dense cathode design, mitigating transport limitations and chemo-mechanical challenges, and ultimately enabling high-rate and long-cycling performance, exceeding that of state-of-the-art composite cathode architectures in SSBs.

3. Conclusion

This study presents a comprehensive investigation of cathode design, featuring densely packed, crystallographically oriented LCO crystals, for next-generation high energy density SSBs. We quantify the theoretical advantages of dense cathodes over composite cathodes and delineate the mechanistic differences between the two architectures. Specifically, crystallographically oriented dense cathode enables rapid, long-range Li diffusion through fast-diffusing facets and provide efficient electronic conduction, eliminating the need for SE and other secondary phases in the cathode microstructure. However, our interrogation also reveals critical interfacial, microstructural, and chemo-mechanical challenges that currently limit the performance of dense cathodes in SSBs. We show that cathode/SE interfacial delamination triggers a pair of interconnected reaction-transport limitations: it causes current focusing at the remaining solid–solid contact points and increases kinetic overpotential at the cathode/SE interface, while also inducing diffusion limitations within the cathode bulk due to hindered Li transport through Li-blocking facets, thereby impacting the cathode performance. We demonstrate that these challenges can be partially alleviated by optimizing the cathode/SE interface morphology and sub-surface microstructure to increase the active area, which lowers the local reaction current densities and enhances the overall cathode utilization. Furthermore, our analysis reveals that microstructural irregularities, such as non-uniform cathode/SE contact distribution, misoriented LCO crystals, pores, and microcracks within the cathode bulk, induce spatiotemporal heterogeneities in lithiation behavior. The resulting heterogeneities not only contribute to capacity reduction but also lead to non-uniform stress accumulation, ultimately leading to the formation of stress hotspots within the cathode. Consequently, these chemo-mechanical implications are identified as the mechanistic bottlenecks for high-rate capability, structural integrity, and long cycle life of dense cathode architectures. Lastly, our comparative analysis reveals that dense cathode architectures outperform composite cathodes in deliverable energy density across all C-rates (0.1C to 1C), with the most significant enhancements of 32.9% in gravimetric energy density and 98.7% in volumetric energy density observed at 1C, demonstrating the potential of dense cathode architectures for faster rate and high energy density applications. Despite the energy density enhancements offered by dense cathodes, this work underscores the crucial need to further optimize dense cathode microstructures to address the chemo-mechanical challenges that currently limit long-term cycling performance. Finally, while this study was based on dense LCO cathodes, our findings provide a foundation for future investigations into dense cathode architectures utilizing other layered oxide materials in SSBs, including $LiNi_xMn_yCo_zO_2$ (NMC) and $LiNi_xCo_yAl_zO_2$ (NCA). In this regard, further research is needed to synthesize and manufacture dense cathode architectures with multiple transition metals (*e.g.*, NMC), where complexities arising from their co-deposition and achieving optimal electrode-level control need to be explored and systematically investigated.

Conflicts of interest

The authors declare no conflicting interests.

Data availability

The data supporting this article have been included as part of the ESI.†

Acknowledgements

References

1 X.-B. Cheng, R. Zhang, C.-Z. Zhao and Q. Zhang, *Chem. Rev.*, 2017, **117**, 10403–10473.
2 J. Liu, Z. Bao, Y. Cui, E. J. Dufek, J. B. Goodenough, P. Khalifah, Q. Li, B. Y. Liaw, P. Liu and A. Manthiram, *Nat. Energy*, 2019, **4**, 180–186.
3 D. Lin, Y. Liu and Y. Cui, *Nat. Nanotechnol.*, 2017, **12**, 194–206.
4 J. Janek and W. G. Zeier, *Nat. Energy*, 2016, **1**, 1–4.
5 J. Huang, K. Wu, G. Xu, M. Wu, S. Dou and C. Wu, *Chem. Soc. Rev.*, 2023, **52**, 4933–4995.
6 S. Li, S. Q. Zhang, L. Shen, Q. Liu, J. B. Ma, W. Lv, Y. B. He and Q. H. Yang, *Adv. Sci.*, 2020, **7**, 1903088.
7 L. Ye and X. Li, *Nature*, 2021, **593**, 218–222.
8 Y.-G. Lee, S. Fujiki, C. Jung, N. Suzuki, N. Yashiro, R. Omoda, D.-S. Ko, T. Shiratsuchi, T. Sugimoto and S. Ryu, *Nat. Energy*, 2020, **5**, 299–308.
9 T. Krauskopf, F. H. Richter, W. G. Zeier and J. R. Janek, *Chem. Rev.*, 2020, **120**, 7745–7794.
10 F. Zhao, Q. Sun, C. Yu, S. Zhang, K. Adair, S. Wang, Y. Liu, Y. Zhao, J. Liang and C. Wang, *ACS Energy Lett.*, 2020, **5**, 1035–1043.

11 M. J. Wang, E. Carmona, A. Gupta, P. Albertus and J. Sakamoto, *Nat. Commun.*, 2020, **11**, 5201.

12 K. G. Naik, B. S. Vishnugopi, J. Datta, D. Datta and P. P. Mukherjee, *Appl. Mech. Rev.*, 2023, **75**, 010802.

13 B. S. Vishnugopi, E. Kazyak, J. A. Lewis, J. Nanda, M. T. McDowell, N. P. Dasgupta and P. P. Mukherjee, *ACS Energy Lett.*, 2021, **6**, 3734–3749.

14 X.-D. Zhang, F.-S. Yue, J.-Y. Liang, J.-L. Shi, H. Li and Y.-G. Guo, *Small Struct.*, 2020, **1**, 2000042.

15 J. Janek and W. G. Zeier, *Nat. Energy*, 2023, **8**, 230–240.

16 P. Minnmann, F. Strauss, A. Bielefeld, R. Ruess, P. Adelhelm, S. Burkhardt, S. L. Dreyer, E. Trevisanello, H. Ehrenberg and T. Brezesinski, *Adv. Energy Mater.*, 2022, **12**, 2201425.

17 K. G. Naik, B. S. Vishnugopi and P. P. Mukherjee, *ACS Appl. Mater. Interfaces*, 2022, **14**, 29754–29765.

18 P. Minnmann, L. Quillman, S. Burkhardt, F. H. Richter and J. Janek, *J. Electrochem. Soc.*, 2021, **168**, 040537.

19 A. Bielefeld, D. A. Weber and J. R. Janek, *ACS Appl. Mater. Interfaces*, 2020, **12**, 12821–12833.

20 F. Walther, S. Randau, Y. Schneider, J. Sann, M. Rohnke, F. H. Richter, W. G. Zeier and J. R. Janek, *Chem. Mater.*, 2020, **32**, 6123–6136.

21 A. Banerjee, X. Wang, C. Fang, E. A. Wu and Y. S. Meng, *Chem. Rev.*, 2020, **120**, 6878–6933.

22 S. Lou, F. Zhang, C. Fu, M. Chen, Y. Ma, G. Yin and J. Wang, *Adv. Mater.*, 2021, **33**, 2000721.

23 K. G. Naik, M. K. Jangid, B. S. Vishnugopi, N. P. Dasgupta and P. P. Mukherjee, *Adv. Energy Mater.*, 2024, 2403360.

24 R. Koerver, I. Aygün, T. Leichtweiß, C. Dietrich, W. Zhang, J. O. Binder, P. Hartmann, W. G. Zeier and J. R. Janek, *Chem. Mater.*, 2017, **29**, 5574–5582.

25 T. Shi, Y.-Q. Zhang, Q. Tu, Y. Wang, M. Scott and G. Ceder, *J. Mater. Chem. A*, 2020, **8**, 17399–17404.

26 P. Barai, T. Rojas, B. Narayanan, A. T. Ngo, L. A. Curtiss and V. Srinivasan, *Chem. Mater.*, 2021, **33**, 5527–5541.

27 L. Li, H. Duan, J. Li, L. Zhang, Y. Deng and G. Chen, *Adv. Energy Mater.*, 2021, **11**, 2003154.

28 S. Wang, R. Fang, Y. Li, Y. Liu, C. Xin, F. H. Richter and C.-W. Nan, *J. Materiomics*, 2021, **7**, 209–218.

29 P. J. Kwon, C. Juarez-Yescas, H. Jeong, S. Moradi, E. Gao, D. Lawrence, B. Zahiri and P. V. Braun, *ACS Energy Lett.*, 2024, **9**, 4746–4752.

30 M. Cronau, M. Duchardt, M. Szabo and B. Roling, *Batteries Supercaps*, 2022, **5**, e202200041.

31 C. Yu, S. Ganapathy, E. R. van Eck, L. van Eijck, S. Basak, Y. Liu, L. Zhang, H. W. Zandbergen and M. Wagemaker, *J. Mater. Chem. A*, 2017, **5**, 21178–21188.

32 F. Strauss, T. Bartsch, L. de Biasi, A.-Y. Kim, J. R. Janek, P. Hartmann and T. Brezesinski, *ACS Energy Lett.*, 2018, **3**, 992–996.

33 T. Shi, Q. Tu, Y. Tian, Y. Xiao, L. J. Miara, O. Kononova and G. Ceder, *Adv. Energy Mater.*, 2020, **10**, 1902881.

34 M. B. Dixit, A. Parejiya, N. Muralidharan, R. Essehli, R. Amin and I. Belharouak, *Energy Storage Mater.*, 2021, **40**, 239–249.

35 C. Park, S. Lee, K. Kim, M. Kim, S. Choi and D. Shin, *J. Electrochem. Soc.*, 2019, **166**, A5318.

36 J. Zhang, H. Zhong, C. Zheng, Y. Xia, C. Liang, H. Huang, Y. Gan, X. Tao and W. Zhang, *J. Power Sources*, 2018, **391**, 73–79.

37 N. C. Rosero-Navarro, T. Kinoshita, A. Miura, M. Higuchi and K. Tadanaga, *Ionics*, 2017, **23**, 1619–1624.

38 S. B. Hong, Y. R. Jang, H. Kim, Y. C. Jung, G. Shin, H. J. Hah, W. Cho, Y. K. Sun and D. W. Kim, *Adv. Energy Mater.*, 2024, 2400802.

39 M. G. Jeong, K. G. Naik, Y. Zheng, W. J. Suk, B. S. Vishnugopi, L. Lin, D. Puthusseri, A. C. Chuang, J. S. Okasinski and J. Sakamoto, *Adv. Energy Mater.*, 2024, 2304544.

40 D. Hlushkou, A. E. Reising, N. Kaiser, S. Spannenberger, S. Schlabach, Y. Kato, B. Roling and U. Tallarek, *J. Power Sources*, 2018, **396**, 363–370.

41 K. G. Naik, B. S. Vishnugopi and P. P. Mukherjee, *Energy Storage Mater.*, 2023, **55**, 312–321.

42 K. G. Naik, D. Chatterjee and P. P. Mukherjee, *ACS Appl. Mater. Interfaces*, 2022, **14**, 45308–45319.

43 L. Cui, S. Zhang, J. Ju, T. Liu, Y. Zheng, J. Xu, Y. Wang, J. Li, J. Zhao and J. Ma, *Nat. Energy*, 2024, 1–11.

44 P. Bouwman, B. A. Boukamp, H. J. Bouwmeester and P. Notten, *J. Electrochem. Soc.*, 2002, **149**, A699.

45 J. Xie, N. Imanishi, T. Matsumura, A. Hirano, Y. Takeda and O. Yamamoto, *Solid State Ionics*, 2008, **179**, 362–370.

46 X. Xu, H. Huo, J. Jian, L. Wang, H. Zhu, S. Xu, X. He, G. Yin, C. Du and X. Sun, *Adv. Energy Mater.*, 2019, **9**, 1803963.

47 S. Wang, X. Zhou, T. Zhao, J. Peng, B. Zhang, W. Xing, M. Zuo, P. Zhang, W. Fan and G. Lv, *Nano Energy*, 2024, **129**, 110008.

48 B. Zahiri, A. Patra, C. Kiggins, A. X. B. Yong, E. Ertekin, J. B. Cook and P. V. Braun, *Nat. Mater.*, 2021, **20**, 1392–1400.

49 N. Wu, Y. Zhang, Y. Guo, S. Liu, H. Liu and H. Wu, *ACS Appl. Mater. Interfaces*, 2016, **8**, 2723–2731.

50 Y. Yoon, C. Park, J. Kim and D. Shin, *J. Power Sources*, 2013, **226**, 186–190.

51 M. Park, X. Zhang, M. Chung, G. B. Less and A. M. Sastry, *J. Power Sources*, 2010, **195**, 7904–7929.

52 A. C. Johnson, A. J. Dunlop, R. R. Kohlmeyer, C. T. Kiggins, A. J. Blake, S. V. Singh, E. M. Beale, B. Zahiri, A. Patra and X. Yue, *J. Power Sources*, 2022, **532**, 231359.

53 M. Ménétrier, I. Saadoune, S. Levasseur and C. Delmas, *J. Mater. Chem.*, 1999, **9**, 1135–1140.

54 H. Mendoza, S. A. Roberts, V. E. Brunini and A. M. Grillet, *Electrochim. Acta*, 2016, **190**, 1–15.

55 X. Gao, B. Liu, B. Hu, Z. Ning, D. S. Jolly, S. Zhang, J. Perera, J. Bu, J. Liu and C. Doerrer, *Joule*, 2022, **6**, 636–646.

56 X. Li, J. Liang, J. Luo, M. N. Banis, C. Wang, W. Li, S. Deng, C. Yu, F. Zhao and Y. Hu, *Energy Environ. Sci.*, 2019, **12**, 2665–2671.

57 C. Rosenbach, F. Walther, J. Ruhl, M. Hartmann, T. A. Hendriks, S. Ohno, J. Janek and W. G. Zeier, *Adv. Energy Mater.*, 2023, **13**, 2203673.

58 A. M. Stavola, X. Sun, D. P. Guida, A. M. Bruck, D. Cao, J. S. Okasinski, A. C. Chuang, H. Zhu and J. W. Gallaway, *ACS Energy Lett.*, 2023, **8**, 1273–1280.

59 H. Sato, D. Takahashi, T. Nishina and I. Uchida, *J. Power Sources*, 1997, **68**, 540–544.

60 H. Xia, L. Lu and G. Ceder, *J. Power Sources*, 2006, **159**, 1422–1427.

61 S. Takeuchi, H. Tan, K. K. Bharathi, G. R. Stafford, J. Shin, S. Yasui, I. Takeuchi and L. A. Bendersky, *ACS Appl. Mater. Interfaces*, 2015, **7**, 7901–7911.

62 D. Chatterjee, K. G. Naik, B. S. Vishnugopi and P. P. Mukherjee, *Adv. Sci.*, 2024, **11**, 2307455.

63 D. K. Singh, A. Henss, B. Mogwitz, A. Gautam, J. Horn, T. Krauskopf, S. Burkhardt, J. Sann, F. H. Richter and J. Janek, *Cell Rep. Phys. Sci.*, 2022, **3**, 101043.

64 W. Li, M. Li, S. Wang, P.-H. Chien, J. Luo, J. Fu, X. Lin, G. King, R. Feng and J. Wang, *Nat. Nanotechnol.*, 2025, **20**, 265–275.

65 A. Hitt, F. Wang, Z. Li, M. Ge, Y. Zhang, Y. Savsatli, X. Xiao, W.-K. Lee, R. Stephens and M. Tang, *Energy Storage Mater.*, 2022, **52**, 320–328.